# Towards Numerical Simulation of Flapping Foils on Fixed Cartesian Grids

M. Bozkurttas*, H. Dong.†, V. Seshadri‡, R. Mittal§
*Department of Mechanical & Aerospace Engineering,*
*The George Washington University,*
*Washington, DC 20052*

*and*

F. Najjar**
*Center for Simulation of Advanced Rockets*
*University of Illinois at Urbana-Champaign*
*Urbana, IL 61801*

**Flapping foils found in nature such as bird and insect wings and fish fins are being studied for potential use in micro aerial vehicles and autonomous underwater vehicles. The fluid dynamics associated with these foils is extremely complicated and much remains to be learnt in this arena. Experimental investigations of flapping foils in nature are limited by their inability to provide full-field, spatially and temporally resolved, velocity and pressure measurements. Many of the limitations can be alleviated with computational fluid dynamics techniques. Computational analysis of these flows is however, by no means an easy proposition due to the many inherent complexities in these flows. These include a wide variety of flow conditions and the presence of flexible moving boundaries. In the current paper, we describe a Cartesian grid based immersed boundary flow solver which is being developed to handle such flows. The paper describes the salient features of the numerical approach along with examples that illustrate its capabilities.**

## I. Introduction

Flapping foils are being considered for lift generation and/or propulsion in Micro Aerial Vehicles (MAVs) and Autonomous Underwater Vehicles (AUVs). Much regarding the fluid mechanics of these biologically inspired flows can be learnt by observing insects, fishes and birds. Experimental investigations of flapping foils in nature are however limited by their inability to provide full-field, spatially and temporally resolved, velocity and pressure measurements[1]. Some of these limitations are associated with the specific conditions imposed by the need to work with live animals since it is difficult to control/predict the motion and location of these animals under test conditions. Also it is usually difficult to instrument the test subjects with sensors to the extent needed without disrupting the natural behavior of the subject. For instance, no method currently exists for extracting surface pressure and shear stress distribution on a structure as delicate as flapping pectoral fin of a fish or flapping wings of insects/birds[2]. Computational fluid dynamics (CFD) on the other hand can overcome many of these limitations and is the method employed in the current study.

This current ongoing effort is specifically focused on understanding the fluid and structural dynamics of a pectoral fin. In particular, the subject of interest here is the bluegill sunfish that has been studied experimentally in detail by Drucker and Lauder[3]. For this fish, the Reynolds number based on fish body length ($L \sim 20$ cm) and velocity ($0.5$ ms$^{-1}$) is about $2\text{x}10^4$. At this Reynolds number, the attached flow over the body is most likely laminar but is expected to transition rapidly to turbulence in regions of flow separation which might occur downstream of appendages. The fins of this fish are also highly flexible, have complex planforms and undergo complicated motions. The flow over the fins can be characterized in terms of a Stokes frequency parameter ( $S = \omega A l / \nu$ ) where $\omega$, $A$

* Graduate Student, AIAA Student Member
† Research Scientist, AIAA Member
‡ Graduate Student
§ Associate Professor, Senior AIAA Member
** Senior Research Scientist, AIAA Member

and $l$ are the fin angular frequency, amplitude and length respectively. Typical fin beat frequency of about 3 Hz and fin amplitude and size of about 2cm and 5cm, respectively; gives $S \approx 1.8 \times 10^4$ that is again in the range where laminar attached flow would quickly transition to turbulence post separation. Thus, assuming that the above conditions are prototypical of bio-hydrodynamic flow configurations, especially in the context of low-speed maneuvering, the key factors to be considered in computational modeling of these configurations are:

**a.** Wide Range of Flow Conditions: Typical Reynolds numbers for swimming fishes/cetaceans can vary from $O(10^2)$ to $O(10^7)$. The flow can be laminar, transitional or turbulent or a combination of all three regimes. In addition, the surrounding flow environment can be steady or unsteady.

**b.** Moving Boundaries: Bio-hydrodynamic flows of interest are often associated with moving boundaries, may they be flapping fins or undulating bodies.

**c.** Two-Way Fluid-Structure Coupling: In many cases the control surfaces (fins, appendages etc) are highly flexible and can undergo large deformations as a result of the hydrodynamic loading (see Fig. 1). This deformation can in turn have a significant effect on the flow, which can then alter the loading itself.

**d.** Unsteady Flow Mechanisms: The presence of moving and flexible control surfaces and/or the unsteady flow environment leads to configurations where dominance of unsteady flow mechanisms (added mass effects, dynamic stall, vortex shedding, vortex pairing, vortex-body and vortex-fin interactions) is a rule rather than an exception.

In the current study, a DNS/LES solver has been developed which is capable of simulating these flows in all their complexity. In particular, the solver, which will be discussed in this study, is time-accurate and non-dissipative, and allows body motion as well as fluid structure interaction. As will be demonstrated here, the non-dissipative property of the solver is the key in allowing us to resolve the vortical features in the flow, which primarily determine the thrust and efficiency of the flapping foils.

Section II discusses the numerical methodology employed in the current solver (hereon referred to as VICAR3D). In Section III performance test results and validation cases are presented. In Section IV, results obtained for several test cases, including fluid structure interaction, LES of circular cylinder, and flapping foils, will be described. Finally Section V provides a summary.

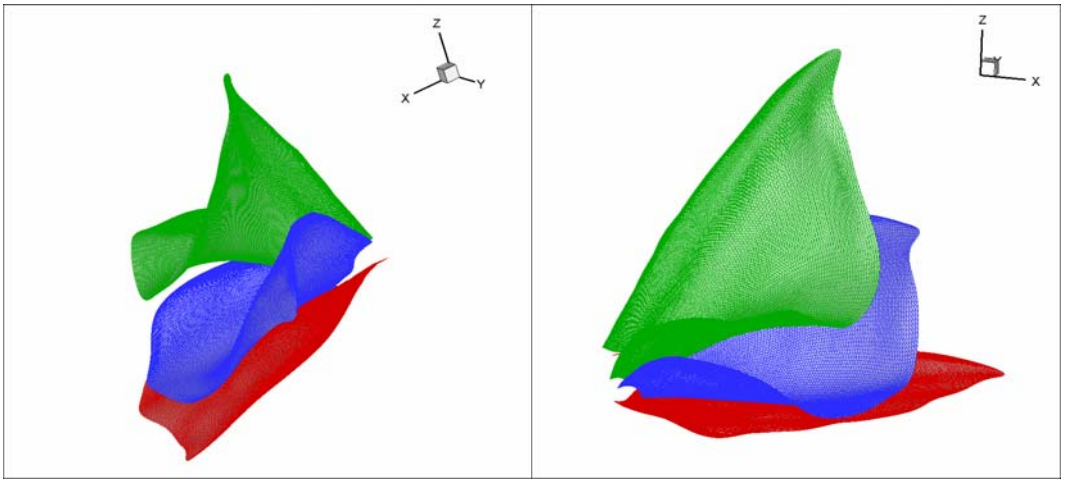


**Figure 1. Two different views of actual kinematics of the pectoral fin of a bluegill sunfish, extracted by Lauder's group at the Harvard University.**

## II. Numerical Methodology

A finite-difference based approach for computing flows with moving immersed solid three-dimensional boundaries on fixed Cartesian grid has been developed. The key feature of this method is that simulations with complex boundaries can be carried out on stationary non-body conformal Cartesian grids and this eliminates the need

for complicated remeshing algorithms that are usually employed with conventional Lagrangian body-conformal methods.

Large-Eddy Simulation (LES) is a viable technique to capture the energy-containing scales of turbulence while modeling the smaller (subgrid) scales. In LES, the flow variables are decomposed into a large-scale (or resolved) component, denoted by overbar, and a subgrid scale component by applying a filtering operation. The filtered Navier-Stokes equations of an incompressible fluid for the resolved field are written in tensor form as:

$$\begin{aligned} &\frac{\partial \bar{u}_i}{\partial x_i} = 0 \\ &\frac{\partial \bar{u}_i}{\partial t} + \frac{\partial \bar{u}_i \bar{u}_j}{\partial x_j} = -\frac{\partial \bar{p}}{\partial x_i} - \frac{\partial \tau_{ij}}{\partial x_i} + \frac{1}{\mathrm{Re}} \frac{\partial^2 \bar{u}_i}{\partial x_j \partial x_j} \end{aligned} \tag{1}$$

where $i$ and $j$ = 1, 2 and 3 correspond to $x$, $y$ and $z$ coordinates, respectively; and Re is the Reynolds number. In the above equations, $\bar{u}_i$ is the instantaneous filtered velocity component in the $i$ direction, $\bar{p}$ represents the filtered pressure, and $t$ is the non-dimensional time. The equations have been non-dimensionalized by appropriate velocity and length scales. Equation (1) describes the transport of the filtered velocity field and contains the contribution of the subgrid scale (SGS) Reynolds stresses, given by $\tau_{ij} = \overline{u_i u_j} - \bar{u}_i \bar{u}_j$. These stresses are formulated using a Boussinesq-based eddy viscosity model:

$$\tau_{ij} - \frac{1}{3}\delta_{ij}\,\tau_{kk} = -2\nu_T \bar{S}_{ij} \tag{2}$$

where $\delta_{ij}$ is the Kronecker delta, and $\bar{S}_{ij} = 1/2\left(\partial \bar{u}_i / \partial x_j + \partial \bar{u}_j / \partial x_i\right)$, corresponds to the filtered strain-rate tensor. A Smagorinsky-type model is used to formulate the eddy viscosity where $\nu_T = \left(C_s \bar{\Delta}\right)^2 \left|\bar{S}\right|$. In this model, $C_s$ is the Smagorinsky constant, which remains to be determined, $\bar{\Delta}$ is a measure of the local grid spacing, and $\left|\bar{S}\right| = \sqrt{2\bar{S}_{ij}\bar{S}_{ij}}$ is the magnitude of the resolved-scale strain rate tensor. Hence, the system of equations will be closed through obtaining an appropriate value of the Smagorinsky constant, $C_s$. Here, a dynamic Lagrangian procedure, formulated by Meneveau et al.[4] is invoked to parameterize the subgrid scale stresses. In the dynamic Lagrangian approach, the model coefficient is averaged along the flow pathlines, and hence requiring no homogeneous direction to maintain numerical stability. The equation for computing the model constant, $C_s$, is:

$$C_s^2(x_i,t) = \frac{\Phi_{LM}}{\Phi_{MM}} \tag{3}$$

where the evolutions of $\Phi_{LM}$ and $\Phi_{MM}$ at time step, (n+1), are given by

$$\begin{aligned} \Phi_{LM}^{(n+1)}(x_i) &= \varepsilon\left[L_{ij}M_{ij}\right]^{(n+1)}(x_i) + (1-\varepsilon)\left[L_{ij}M_{ij}\right]^{(n)}\left(x_i - \bar{u}_i \Delta t\right) \\ \Phi_{MM}^{(n+1)}(x_i) &= \varepsilon\left[M_{ij}M_{ij}\right]^{(n+1)}(x_i) + (1-\varepsilon)\left[M_{ij}M_{ij}\right]^{(n)}\left(x_i - \bar{u}_i \Delta t\right) \\ \varepsilon &= \frac{\Delta t / T^n}{1 + \Delta t / T^n} \end{aligned} \tag{4}$$

where $T^n$ is a representative timescale taken to be either, $T^n = 3/2\bar{\Delta}\left(\Phi_{LM}^n \Phi_{MM}^n\right)^{-1/8}$ [see Ref. 4] or $T^n = \left|\bar{S}\right|^{-1}$. The variables, $L_{ij}$ and $M_{ij}$, are defined through the Germano's identity, given in Ref. 5, as follows:

$$\begin{aligned} L_{ij} &= \widehat{\bar{u}_i \bar{u}_j} - \hat{\bar{u}}_i \hat{\bar{u}}_j \\ M_{ij} &= 2\bar{\Delta}^2 \left( \widehat{\left|\bar{S}\right| \bar{S}_{ij}} - 4 \left|\hat{\bar{S}}\right| \hat{\bar{S}}_{ij} \right) \end{aligned} \tag{5}$$

The hat represents a secondary filtering operation, called test filter, and is usually applied on twice the size of the grid spacing. The equations are integrated in time using the fractional step method [6]. This approach follows along the lines of that used by Mittal & Balachandar[7] and Mittal[8]. In the first step, an intermediate velocity field, $\tilde{u}_i$, is calculated from the momentum equations without the contribution of the pressure gradient. In the second step, the pressure field

is computed by solving a Poisson equation. The divergence-free velocity field, $\bar{u}_i^{n+1}$, is then obtained by correcting the intermediate velocity field with the computed pressure gradient. In the current solution procedure, the convective terms are represented using an explicit Adams-Bashforth scheme; while the diffusive terms are modeled with an implicit Crank-Nicolson procedure.

The spatial derivatives have been discretized with a second-order accurate central difference scheme on a collocated finite-difference stencil. In the collocated-grid arrangement, all variables (i.e., velocity components and pressure) are located at the same physical location in contrast to the staggered node arrangement where the velocities are centered with the pressure locations. For the pressure-Poisson equation, the gradient term uses a compact second-order central difference stencil. The solution of pressure Poisson equation (PPE) is the most time consuming part of the solution algorithm. In the current solver an efficient multigrid methodology has been developed which is well suited for use in conjunction with the immersed boundary method. The details of this method will be discussed in Section III. In addition to the cell-centered nodal velocities, we separately carry and update the face normal velocities. This allows us to satisfy the divergence-free condition to machine accuracy (see Ref. 9 for further details).

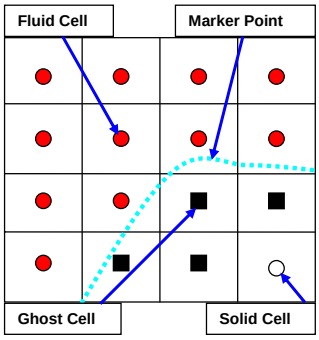


**Figure 2. Designation of various nodes on the grid.**

The general framework for handling moving immersed boundaries can be considered as an Eulerian-Lagrangian formulation, wherein the immersed boundaries are explicitly tracked as surfaces in a Lagrangian mode, while the flow computations are performed on a fixed Eulerian mesh. The geometry of the immersed boundary is defined by a set of "marker points" as shown in Fig. 2. Cells whose centers lie inside the immersed body and have at least one neighboring cell, whose cell center lies outside the body, are marked as "ghost cells"[10]. The rest of the cells with centers inside the body and not adjacent to immersed boundary, are marked as "solid cells". Figure 2 shows the marker points, fluid cells, ghost cells and solid cells for an immersed boundary on Cartesian grid. The basic idea in this method is to compute the flow variables for the ghost cells such that boundary conditions on the immersed boundary in the vicinity of the ghost cell are satisfied[10]. To compute the value at ghost cell center, a "normal probe" is extended from this node to the immersed boundary (to a point called "boundary intercept" point) and is extended further into fluid to a point, which we call "probe tip". Four cell nodes (for the 2D case), which surround the probe tip are then identified and a bilinear interpolation is employed to calculate values at the probe tip. The variables at the corresponding ghost node are subsequently computed by extrapolating them from the probe-tip and boundary-intercept points such that they satisfy appropriate Dirichlet or Neumann's boundary conditions on the boundary intercept point. Two approaches are used based on if four cell centers that surround the tip-marker point include the ghost cell center or not. Figure 3a and Fig. 3b show these approaches schematically. An earlier implementation of this approach for compressible flow can be found in Ghias et al.[10]

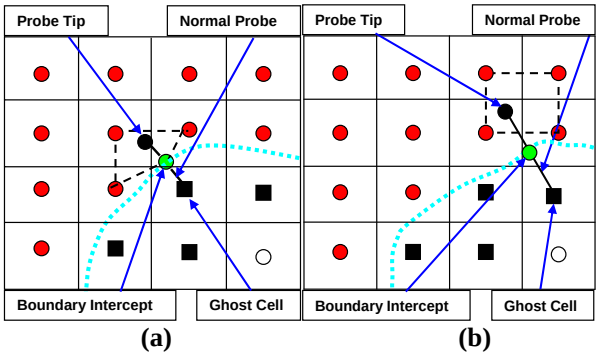


**Figure 3. Interpolation stencils employed for the ghost cells.**

## III. Performance Test and Validation

### A. Multi-Grid Method

The key elements of a multigrid procedure are (i) an appropriate smoother, (ii) grid coarsening, (iii) restriction, (iv) prolongation, and (v) multigrid schedule. The implementation of a standard multigrid algorithm into the current solver would at first glance seem straightforward given the simple mesh topology. However, implementation of the multigrid method requires the reconstruction of the immersed boundary at every coarse multigrid level, which can significantly increase the complexity of the scheme. Moreover, the total number of grid points in all three directions is quite different in most of our computations. Therefore, a nonstandard geometric multigrid method with a flexible semi-coarsening strategy [11,12] has been developed for the PPE. The primary complexity in applying a multigrid technique in the current solver is associated with retaining the immersed boundary as a sharp interface at the coarse

grid levels at each direction. Motivated by this, a multigrid algorithm has been developed wherein the boundary is represented as a sharp interface only at the finest grid level. At the coarser levels, the presence of the boundary is accounted for only in an approximate sense through the volume fraction of the coarse cells and no explicit reconstruction of the immersed boundary is done at these levels. Although conceptually straightforward, it is essential to ensure that this approach not degrade the convergence properties of the underlying multigrid algorithm.

Performance tests of the multigrid method have been carried out on a 2.8 GHz Pentium-IV cluster for a canonical case involving two circular cylinders immersed in a square computational domain. The focus is on comparing the performance of the current multigrid with PetSc (developed at Argonne National Lab), which is a state of art GMRES based solvers[13]. Simulations on various size grids have been carried out to examine how the performance of these different methods scales with grid size (N). Note that we expect CPU time to scale with $N^2$ for a non-accelerated iterative method like Jacobi or Gauss-Siedel while the theoretical performance of a multigrid should approach $N^1$. We find that for the current code, PetSc performance scales roughly with $N^{1.78}$ which is somewhat better than the typical iterative methods. On the other hand, the multigrid method developed here scales with $N^{1.17}$ which is a substantial improvement over the PetSc performance. It should also be noted that the observed performance of the multigrid method is reasonably close to the ideal theoretical performance thereby confirming that the current multigrid is highly effective when used with VICAR3D.

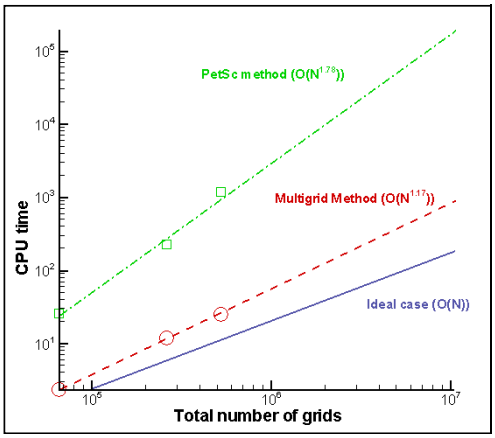


**Figure 4. Observed and projected performance of PetSc and current multigrid method with the number of grid points (N)**

## B. Demonstration of Spatial Accuracy

A systematic grid refinement study has been carried out to demonstrate that the ghost-cell methodology maintains its second-order accuracy globally as well as locally. Two-dimensional flow past a cylinder is solved in $2d \times 2d$ square domain at Re = 100 (where Reynolds number is, $\mathrm{Re} = U_\infty d / \upsilon$; $d$ is the diameter of the cylinder, $U_\infty$ is the freestream velocity and $\upsilon$ is kinematic viscosity) with a sequence of grids starting from the finest grid size 316×316 and coarsening by a factor of 3, 5 and 7. $L_1$, $L_2$ and $L_\infty$ norm errors are calculated for the velocities ($u$ and $v$) on the three coarser grids in reference to the solution on the finest grid. The error norms, shown in Fig. 5, clearly demonstrate the second-order accuracy of the current ghost-cell methodology.

## C. Moving Boundary Simulations

Flows of interest in this study are associated with moving boundaries, such as flapping foils or undulating bodies as stated before. Here we demonstrate the accuracy of the current method for flows with moving boundaries by simulating flow past an impulsively started normal flat plate at a Reynolds number of 126 based on the length of the plate.

Rather than simulate impulsively started flow past a stationary plate as has been done before, we simulate the flow associated with a plate impulsively moved in an otherwise stationary fluid. The resulting flow in these two situations should be the same when viewed in the appropriate reference frame and this allows us to examine the fidelity and accuracy of our moving boundary algorithm.

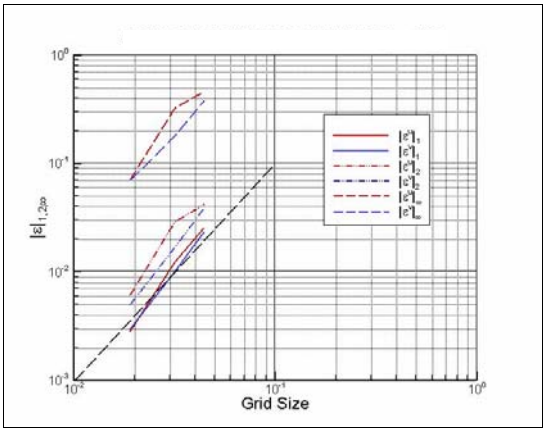


**Figure 5. Test of spatial accuracy for VICAR3D**

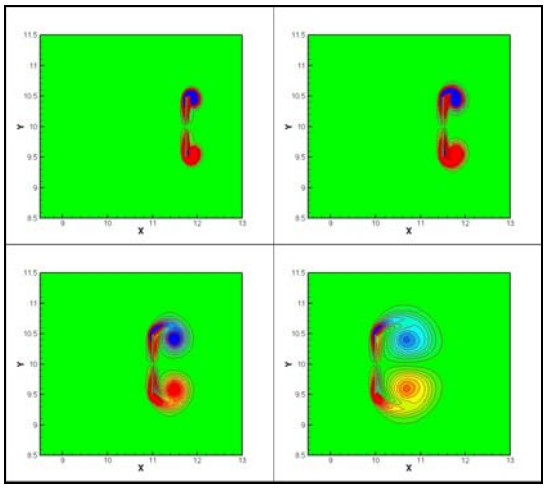

**Figure 6. Spanwise vorticity contours for an impulsively started normal plate at Re = 126**

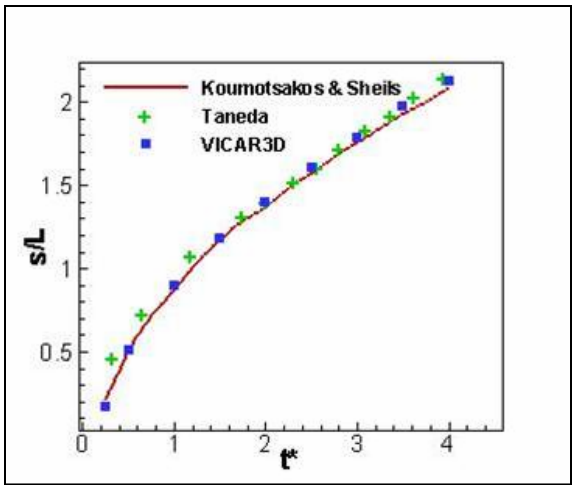


**Figure 7. Evolution of the wake bubble size behind impulsively started flat plate at Re = 126**

Figure 6 shows the unsteady, early time development of the vortices formed behind the plate at four time instances, where $t^*$ is non-dimensional time defined as, $t^* = Ut / L$. An extensive study had been carried out on the same flow by Ref. 14 using an accurate vortex method. In Fig. 7, the length of the recirculating bubble, as computed by the present method, is compared with the experimental results of Taneda and Honji[15] and computations of Koumoutsakos and Shields[14]. At the early time stages demonstrated in Fig. 7, VICAR3D results are seen to be in good agreement with the experimental data and those obtained with the vortex method.

## IV. Results

### A. Fluid Structure Interaction

Due to the flexibility/deformability of fish fins, fluid-structure interaction is an essential feature of these flows. Therefore, the ability to simulate two-way coupled fluid structures interaction is needed. Here we demonstrate the ability of VICAR3D to handle such problems by simulating a canonical flow; flow induced transverse vibration in a elastically mounted circular cylinder placed in a freestream.

For this flow, the Navier-Stokes equations are solved in a loosely coupled manner with the equations governing the motion of the cylinder. At the end of each time step, body velocity is updated by using the Newmark scheme[16]. Based on the new velocities, the latest position is calculated and subsequently the body is moved over to its new position.

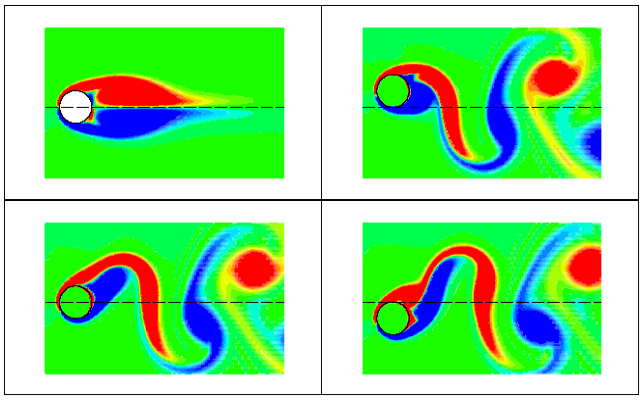

**Figure 8. Vortex shedding behind an elastically mounted cylinder, constrained to move vertically.**

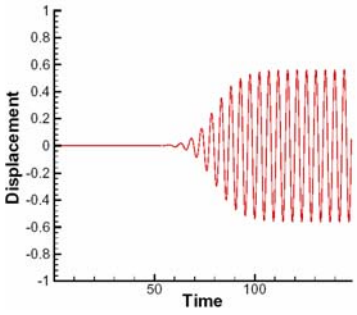


**Figure 9. Displacement time history for cylinder.**

Figure 8 shows the spanwise vorticity field at four time instances. The dashed line corresponds to its undisturbed location and the sequence of plots clearly shows the significant flow induced oscillations that are produced by the vortex shedding. Figure 9 illustrates the time history of displacement of the cylinder, which shows that the oscillations initially increase in amplitude but eventually saturate to a constant amplitude.

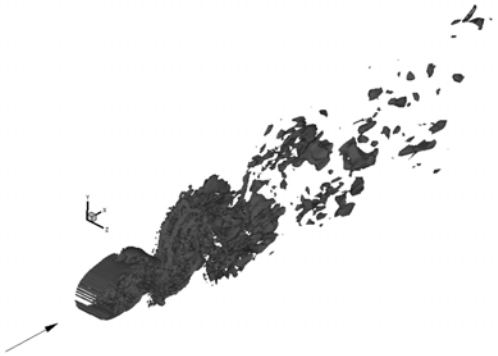

**Figure 10. Isosurfaces of swirl strength for the flow past a circular cylinder at Re = 1500.**

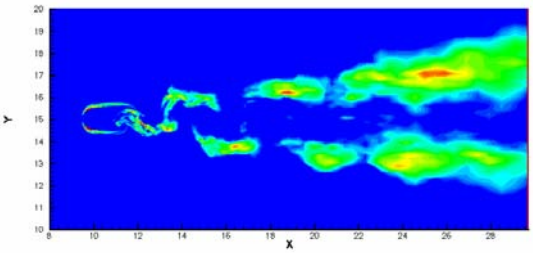

**Figure 11. Contours of turbulent viscosity normalized by molecular viscosity.**

### B. Large Eddy Simulation (LES) Results

To demonstrate the LES capabilities of the present solver, the flow past a circular cylinder is simulated using the dynamic Lagrangian model at a moderate Reynolds number of 1500. The computational domain extends 30 diameters in the streamwise and cross-streamwise directions while the spanwise length is one diameter with the cylinder placed halfway in the domain. The grid consists of 0.46 million points, non-uniformly distributed in the streamwise and transverse directions. Figure 10 shows the isosurfaces of the instantaneous swirling strength. The initial rollup of the Karman vortices close to the cylinder and formation of streamwise rib vortices is clearly captured. Figure 11 shows the turbulent viscosity at the mid-plane ($z/D = 0.5$). It is seen that as expected, the LES model predicts high values of turbulent viscosity in regions of significant three-dimensionality.

### C. Pitching Foil Simulations

Finally we present simulations of flow past a flapping foil. The flow around a NACA 0012 foil undergoing pitch oscillation at a chord Reynolds number of 12,600 has been investigated by Koochesfhani and Bohl[17] using molecular tagging velocimetry (MTV) technique. In this experiment, the airfoil is oscillated sinusoidally about its quarter chord axis with pitch amplitudes of 2 and 4 degrees and with frequency $f$ in the range 1.18-3.21 Hz. A well-defined array of isolated vortices is observed in the wake of the pitching foil at small amplitude and high frequencies. The vertical alignment of the vortices is a function of the reduced frequency parameter $k$ (where $k = \pi f c/U_\infty$, $c$ is the foil chord, $f$ is the frequency and $U_\infty$ is the freestream velocity) with the orientation switching at for $k > 5.7$. The switch in vertical orientation is marked by a change in the mean streamwise velocity from a velocity deficit to a velocity excess (jet like) profile[17]. Also, airfoil mean thrust coefficient as a function of reduced frequency for both 2° and 4° pitch amplitudes has been acquired in Ref. 17.

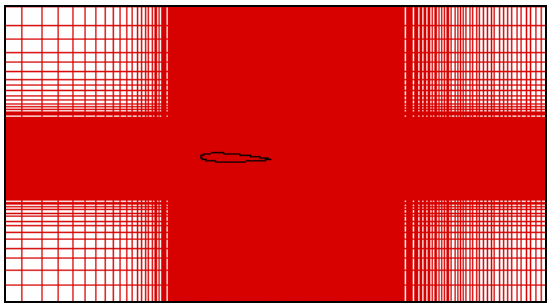

**Figure 12. Cartesian grid used for pitching NACA 0012 airfoil simulation at Re = 12,600.**

In the present study, two-dimensional simulation of this flow has been carried out in which the pitch motion of a foil is prescribed as follows:

$$\alpha = \alpha_1 \sin\left(2\pi f t\right)$$

where, $\alpha_1$ is the amplitude of the sinusoidal pitch angle variation and $f$ is the pitching frequency. In addition to $\alpha_1$, the non-dimensional parameters that govern the fluid dynamics of this configuration are the Reynolds number $Re_c = U_\infty c/\upsilon$ (where $U_\infty$ is the freestream velocity, $c$ is the foil chord and $\upsilon$ is the kinematic viscosity of the fluid) and the Strouhal number $St = fh_1/U_\infty$ based on the wake width (where $h_1$ is the wake width). An alternative frequency parameter based on the foil chord is the reduced frequency which is defined as, $k = \pi f c/U_\infty$.

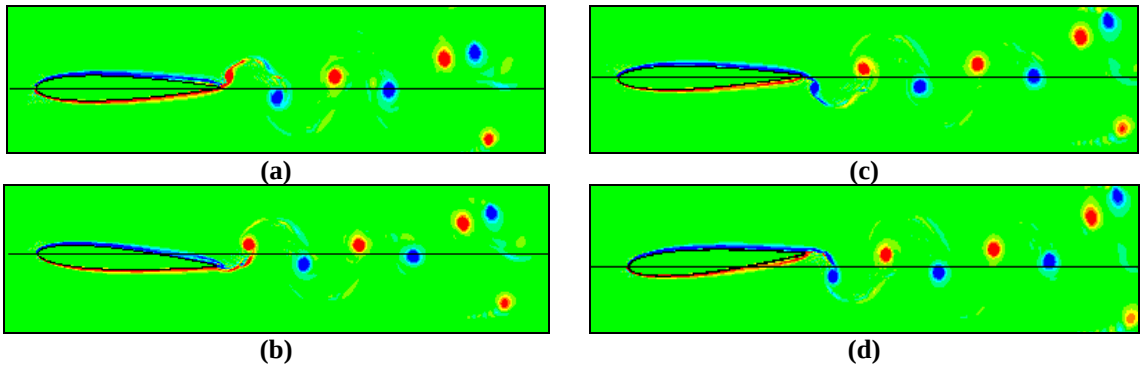


**Figure 13. Spanwise vorticity contours of pitching NACA 0012 with $\alpha_1 = 4°$ at $k = 5.7$ and Re = 12,600 for (a) $\alpha = 0°$ (b) $\alpha = 4°$ (c) $\alpha = 0°$ (d) $\alpha_o = -4°$**

A 519×301 grid is used in the current simulation and the computational domain size is $8.0c \times 6.0c$ (Fig. 12). Since, experiments clearly show that vortex dynamics in the wake often times holds the key to the performance of flapping foils [3,19,20,21], high grid resolution is provided around the foil and through the wake. Figure 13 demonstrates the presence of an inverse Karman vortex which is indicative of thrust production at $k = 5.7$ for 4 degrees pitch amplitude case.

Figure 14 shows the time variations of hydrodynamic force coefficients $C_T$ and $C_L$, where the thrust and lift coefficients are defined as $C_T = F_x / \frac{1}{2}\rho U^2 A_{plan}$ and $C_L = F_y / \frac{1}{2}\rho U^2 A_{plan}$, respectively. Computed mean thrust coefficients are compared with experimental values of Koochesfehani and Bohl[17] and RANS computations of Ramamurti and Sandberg[18] in Fig. 15. Comparison with the experiment indicates significant under-prediction of the thrust although good match is observed with the 2D RANS calculation. This discrepancy could be related to the absence of 3D effects in both numerical simulations. An initial study has been done using VICAR3D to analyze the effect of three dimensionality on the force calculations at a Reynolds number of 1000. Although there is an indication of the generation of streamwise vortical structures in the wake of this thrust producing flapping foil, the inclusion of 3D effects does not seem to effect force calculations at least at this Reynolds number.

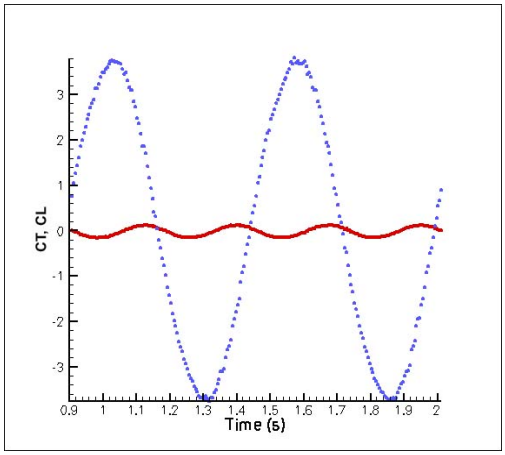


**Figure 14. Time variations of hydrodynamic force coefficients $C_T$ (solid line) & $C_L$ (dotted line) for pitching NACA0012 with $\alpha_1 = 4°$ and $k = 5.7$ & at Re = 12,600**

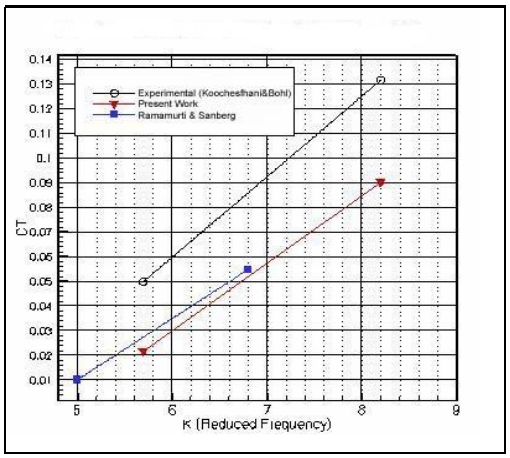


**Figure 15. Comparison of thrust coefficients with Bohl and Koochesfahani's experimental[17] and Ramamurti and Sandberg's numerical results[18] ($\alpha_1 = 4°$)**

Other possibilities that might cause a discrepancy between experimental and numerical work had been studied by Ramamurti and Sandberg[18]. They estimated the force coefficients by integrating the velocity profile at the downstream of the airfoil as has been done in the experiments. Their results showed that the force values estimation

from the wake integral is quite sensitive to wake location. They have also investigated computationally the effect of the presence of tunnel walls. The tunnel walls were found to marginally increase the thrust coefficient[17]. It should be pointed out that while Ramamurti and Sandberg compared their results with the earlier experiments of Koochesfhani[21] whereas in the current paper the comparison has been done using their most recent results[17], which includes the effect of fluctuating components and pressure gradient in the wake. Despite the improved force estimation technique employed in the experiment, the discrepancy between experiment and simulations remains.

## V. Summary

A Cartesian grid based immersed boundary solver has been developed to simulate, among other things, the flow associated with complex flapping foils found in nature. Several validation cases have been described showcasing the fidelity, accuracy and efficiency of this solver for complex flows. Cases involving fluid-structure interaction as well as LES of moderately high Reynolds number flows are also presented in order to demonstrate the capabilities of the solver. Application of this method to complex flapping foils will be presented in the future.

## Acknowledgment

This is work is supported under ONR Grant N00014-03-1-0897.

## References

[1]F. E. Fish, G. V. Lauder, R. Mittal, A. H. Techet, M. S. Triantafyllou, J. A. Walker, and P. W. Webb., "Conceptual Design for the Construction of a Biorobotic AUV Based on Biological Hydrodynamics," *Proceedings of 13th International Symposium on Unmanned Untethered Submersible Technology (UUST)*, Durham, New Hampshire, 2003.

[2]Mittal, R., "Computational Modeling in Bio-hydrodynamics: Trends, Challenges and Recent Advances," *13th International Symposium on Unmanned Untethered Submersible Technology*, August 2003.

[3]Drucker, E. and Lauder, V., "Experimental hydrodynamics of fish locomotion: functional insights from wake visualization," *Integ. and Comp. Biol.*, Vol. 42, 2002, pp. 243-257.

[4]Meneveau, C., Lund, T.S., and Cabot, W.H., "A Lagrangian dynamic subgrid-scale model of turbulence," *J. Fluid Mechanics*, Vol. 319, 1996, pp. 353-385.

[5]Germano, M,. Piomelli, U., Moin, P., and Cabot, W.H., "A dynamic subgrid-scale eddy viscosity model," *Phys. Fluids*, Vol. 3, 1991, pp. 1760-1765.

[6]Chorin, A.J., "A Numerical Method for Solving Incompressible Viscous Flow Problems," *J. Comp. Phys.*, Vol. 2, 1967.

[7]Mittal, R. and Balachandar, S., "Direct Numerical Simulation of Flow Past Elliptic Cylinders," *J. Comp. Phys.*, Vol. 124, pp. 351-367, 1996, pp. 12-26.

[8]Mittal, R., "A Fourier-Chebyshev Spectral Collocation Method for Simulating Flow past Spheres and Spheroids," *Int. J. Num. Meth. Fluids*, Vol. 30, 1999, pp. 921-937.

[9]Zang, Y., Streett, R.L., and Koseff, J.R., "A Non-Staggered Fractional Step Method for Time-Dependent Incompressible Navier-Stokes Equations in Curvilinear Coordinates," *J. Comp. Phys.*, Vol. 114, 1994, pp. 18.

[10]Ghias, R., Mittal, R, and Lund, T.S., "A non conformal grid method for simulation of compressible flows with complex immersed boundaries," *AIAA Paper 2004-0080*, 2004.

[11]Piquet, J. and Vasseur, X., "A nonstandard multigrid method with flexible multiple semi coarsening for the numerical solution of the pressure equation in a Navier-Stokes solver," *Numerical Algorithms* , Vol.24, 2000, pp. 333-355.

[12]Schaffer, S., "A semi coarsening multigrid method for elliptic partial differential equations with highly discontinuous and anisotropic coefficients," *SIAM J. Sci. Comput.*, Vol. 20, 1998, pp. 228-242.

[13]Balay, S., Buschelman, K., Eijkhout, V., Gropp, W., Kaushik, D., Knepley, M., McInnes, L. C., Smith, B. and Zhang, H., *PETSc Users Manual*, August 2003.

[14]Koumoutsakos, P. and Shields, D., "Simulations of the viscous flow normal to an impulsively started and uniformly accelerated flat plate," *J. Fluid Mech.*, Vol. 328, 1996, pp. 177-227.

[15]Taneda, S. and Honji, H., "Unsteady flow past a flat plate normal to the direction of motion," *J. Phys. Soc. Japan*, Vol.30, 1971, pp. 262.

[16]Cook, R.D., Malkus, D.S, Plesha, M.E., and Witt, J.R., *Concepts and Applications of Finite Element Analysis*, 4 th. Edition, Wiley.

[17]Bohl, D.G. and Koochesfhani, M.M., "MTV Measurements of the flow structure downstream of an oscillating airfoil," *AIAA Paper 2003-4017*, 2003.

[18]Ramamurti, R. and Sandberg, W. C., "Simulation of Flow About Flapping Airfoils Using a Finite Element Incompressible Flow Solver,"*AIAA J.*, Vol. 39, No. 2, 2001, pp. 253-260.

[19]Tuncer, I. H. and Platzer, M. F., "Computational Study of Flapping Airfoil Aerodynamics," *AIAA J. of Aircraft*, Vol. 37, No.3, May-June 2000, pp. 514-520.

[20]Anderson, J.M., *Vorticity Control for Efficient Propulsion*, PhD Thesis, Massachusetts Institute of Technology, 1996.

[21]Koochesfahani, M.M., "Vortical Patterns in the Wake of an Oscillating Airfoil," AIAA 25th Aerospace Sciences Meeting, Reno, NV, Jan. 12-15 1987.